

AN EXPERIMENTAL AND NUMERICAL INVESTIGATION OF SHOCK-WAVE INDUCED  
TURBULENT BOUNDARY-LAYER SEPARATION AT HYPERSONIC SPEEDS<sup>†</sup>

By J. G. Marvin, C. C. Horstman, M. W. Rubesin,  
T. J. Coakley, and M. I. Kussoy

NASA Ames Research Center

SUMMARY

This paper describes a thoroughly documented experiment that was specifically designed to test and guide computations of the interaction of an impinging shock wave with a turbulent boundary layer. Detailed mean flow-field and surface data are presented for two shock strengths which resulted in attached and separated flows, respectively. Numerical computations, employing the complete time-averaged Navier-Stokes equations along with algebraic eddy-viscosity and turbulent Prandtl number models to describe shear stress and heat flux, are used to illustrate the dependence of the computations on the particulars of the turbulence models. Models appropriate for zero-pressure-gradient flows predicted the overall features of the flow fields, but were deficient in predicting many of the details of the interaction regions. Improvements to the turbulence model parameters were sought through a combination of detailed data analysis and computer simulations which tested the sensitivity of the solutions to model parameter changes. Computer simulations using these improvements are presented and discussed.

INTRODUCTION

The availability of larger, faster computers, the need to reduce wind-tunnel testing, which is time consuming and costly, and the need to provide alternate simulation capability for test conditions beyond the reach of practical wind-tunnel design have resulted in increased emphasis on computational fluid mechanics. Computations that were not feasible several years ago are

<sup>†</sup> Paper to be presented at the Symposium On Flow Separation sponsored by the AGARD Fluid Dynamics Panel at Göttingen, Germany, 27-30 May, 1975.

now being performed routinely. For example: inviscid three-dimensional computations for speeds ranging from transonic to hypersonic are possible (refs. 1 and 2); even flows where dominant viscous interactions occur, such as the interaction of a shock with a boundary layer, are being computed (refs. 3 and 4). These interacting flows present the greatest challenge, however, because most of the practical applications occur at high Reynolds numbers where the flow is turbulent and little is known about turbulence modeling.

Until recently, most of the techniques for predicting the flow behavior in the vicinity of shock boundary-layer interactions were based on experimental correlations or approximate solutions to the boundary-layer equations. But advances in numerical methods and increased computer speed and capacity have resulted in successful attempts to obtain steady-state solutions of the complete time-dependent Navier-Stokes equations. Computations of laminar interactions have been used to illustrate the utility and accuracy of these techniques (refs. 3 and 4). Very recent examples for turbulent flows (refs. 5-7) illustrate that such computations using the time-dependent, time-averaged Navier-Stokes equations<sup>†</sup> are also feasible and that they describe the qualitative features of the flow interactions. In these examples, closure of the conservation equations was accomplished by describing the turbulent shear stress and heat flux by eddy-viscosity models and turbulent Prandtl numbers. However, a lack of sufficient detailed experimental data precluded verification of these models and efforts to modify them so that the quantitative flow features could be more aptly described.

The present study was undertaken to provide a formidable first step toward understanding the mechanisms that must be modeled before successful numerical calculations of these complicated flows can be made. It combines experimental and numerical methods to guide and verify turbulence modeling for two shock boundary-layer interaction flows, one with and one without separation. An axisymmetric experimental arrangement was chosen to assure purely two-dimensional flow (ref. 8). Shocks of two different strengths were impinged on an established turbulent boundary layer to set up both unseparated and separated flows in the interaction zone. Detailed measurements, consisting of surface-pressure, skin-friction, heat-transfer, and boundary-layer profiles of velocity, static pressure, and temperature were obtained at finely spaced intervals along the surface. Analysis of these data was undertaken to define the detailed behavior of the turbulence parameters used to describe the shear stresses throughout the interaction regions. Computations were made using the time-dependent, time-averaged Navier-Stokes equations employing the exact experimental boundary conditions and algebraic eddy-viscosity descriptions for the turbulent shear stress. The authors reported preliminary progress on the separated case in reference 9.

---

<sup>†</sup>Time averaging in these equations is over periods long compared to turbulence time scales, but short compared to the time variations of the flow field as a whole.

## NOTATION

- $A, A_w^+$  Van Driest damping parameter, Eqs. (5) and (6)
- $c_p$  specific heat at constant pressure
- $c_v$  specific heat at constant volume
- $C_F$  local skin friction coefficient,  $\tau_w / (1/2)\rho_\infty u_\infty^2$
- $C_H$  local Stanton number,  $q_w / \rho_\infty u_\infty c_p (T_t - T_w)$
- $e$  total specific energy per unit volume,  $\rho [c_v T + (v^2 + u^2) / 2]$
- $F, G, H$  mass-averaged fluxes, Eqs. (1) and (2)
- $I$  intermittency factor, Eq. (9)
- $k$  thermal conductivity
- $l$  mixing length, Eqs. (4) and (20)
- $p$  time-averaged pressure
- $Pr$  molecular Prandtl number,  $\mu c_p / k$
- $Pr_t$  turbulent Prandtl number
- $q_x$  axial heat flux,  $-c_p (\mu / Pr + \rho \epsilon / Pr_t) \partial T / \partial x$
- $q_r, q$  radial heat flux,  $-c_p (\mu / Pr + \rho \epsilon / Pr_t) \partial T / \partial r$
- $r$  radial coordinate, distance from model centerline
- $t$  time
- $T$  temperature
- $u$  mass-averaged velocity component in axial direction
- $U$  mass-averaged conservation variables, Eqs. (1) and (2)
- $v$  mass-averaged velocity component in radial direction
- $x$  axial coordinate, distance from leading edge of shock-wave generator
- $y$  distance normal to model surface
- $\alpha$  shock-wave generator leading-edge angle

$\delta$	boundary-layer thickness
$\delta_0$	boundary-layer thickness at the upstream location of the first measured profile station
$\delta_i^*$	kinematic displacement thickness, Eq. (8)
$\delta_c^*$	compressible displacement thickness, Eq. (11)
$\epsilon$	eddy viscosity, Eqs. (4) and (20)
$\kappa$	Von Kármán constant, Eq. (5)
$\mu$	viscosity
$\rho$	time-averaged density
$\sigma_r$	radial normal stress, $p - 2\mu_T \frac{\partial v}{\partial r} + \frac{2}{3} \mu_T \left( \frac{v}{r} + \frac{\partial v}{\partial r} + \frac{\partial u}{\partial x} \right)$
$\sigma_x$	axial normal stress, $p - 2\mu_T \frac{\partial u}{\partial x} + \frac{2}{3} \mu_T \left( \frac{v}{r} + \frac{\partial v}{\partial r} + \frac{\partial u}{\partial x} \right)$
$\sigma_\theta$	azimuthal normal stress, $p - 2\mu_T \frac{v}{r} + \frac{2}{3} \mu_T \left( \frac{v}{r} + \frac{\partial v}{\partial r} + \frac{\partial u}{\partial x} \right)$
$\tau, \tau_{xr}$	total shear stress, Eq. (3)

### Subscripts

f	final axial grid location
i	initial axial grid location
max	maximum
o	location of incident shock impingement on cylinder surface in the absence of a boundary layer
r	radial direction
t	stagnation conditions
T	total
x	axial direction
w	wall
$\infty$	local free stream ahead of interaction

## APPARATUS AND PROCEDURES

### Facility

The experiment was conducted in the NASA Ames Research Center 3.5-Foot Hypersonic Wind Tunnel. This facility operates in a blowdown mode and utilizes contoured axisymmetric nozzles to achieve a uniform Mach number, and an open-jet type test core approximately 0.7 m in diameter and 4 m in length. The present tests were all performed at a nominal free-stream Mach number of 7.2 and with nominal values of total temperature and pressure of 695 K and 34 atmospheres, respectively. The corresponding nominal value of free-stream unit Reynolds number was  $10.9 \times 10^6 \text{ m}^{-1}$  and the useful test time was about 3 min.

### Model

A cone-ogive cylinder, 330 cm in length and 20.3 cm in diameter was used as the test surface (see fig. 1). An annular shockwave generator, 51 cm in diameter, mounted concentric with the cylinder axis was used to generate shock waves of two different strengths by beveling the sharp leading edge at either  $7.5^\circ$  or  $15^\circ$ . The generator could be translated in a direction parallel to the cylinder axis so that the entire interaction region could be passed over selected survey stations.

Interchangeable instrumentation ports, 12 cm in diameter and specifically contoured to match the cylindrical surface, were located at 25 cm intervals along the cylinder in a single line, and every 50 cm in another line  $180^\circ$  around the body. One port was instrumented with a floating element skin-friction balance. Another was used to accommodate either pitot and static pressure probes or total temperature probes. The probes were positioned by a mechanism contained inside the cylinder and automatically actuated from outside the tunnel test section. The remaining ports were instrumented with thermocouples spot-welded to the inner surface every 1.25 cm and with static pressure taps. Static pressure taps were also located every 5 cm along the entire cylinder between ports.

### Test Procedure

Data were collected from a series of tests with the tunnel operating at the nominal conditions described above. In separate tests without the generator it was determined that a fully developed turbulent boundary layer with negligible axial pressure gradient was established over the cylinder surface between 100 and 300 cm from the model tip (ref. 10). With the generator in place, the nominal measured boundary-layer parameters ahead of the interaction for the  $7.5^\circ$  and  $15^\circ$  generator angles, respectively, were: edge Mach number, 6.7 and 6.9; boundary-layer thickness, 3.2 cm and 2.7 cm; and Reynolds number based on boundary-layer thickness,  $0.23 \times 10^6$  and  $0.2 \times 10^6$ . The model wall temperature was essentially constant at a value of 300 K.

Surface pressure, skin friction, and heat transfer were obtained at small intervals by moving the shock-wave generator in an axial direction during the tests. The boundary-layer thickness increased about 10% over the distance of 25 cm which corresponded to the difference between the farthest upstream and downstream positions of the generator. The difference in boundary-layer thickness had little influence on the results, provided they were compared at equivalent distances from the leading edge of the generator.

Skin friction was measured with a contoured floating-element balance whose sensible element was 0.95 cm in diameter. Calibrations of the gage before and after each test run were repeatable to within 5%. The skin-friction data were corrected for buoyancy effects resulting from the axial pressure gradient. Corrections were less than 10% of the measured values, except in the regions of minimum skin friction for the  $7.5^\circ$  generator tests and near separation and reattachment for the  $15^\circ$  generator tests, where they were as high as 50% of the measured upstream zero pressure gradient values. The heat-transfer rate was measured using the thin-wall transient technique. Longitudinal conduction errors were computed and found to be less than 5% of the measured rates and so no corrections were applied to these data.

Velocity, density, and pressure profiles were obtained from pitot and static pressure and total temperature surveys. Each survey was taken during a single test run, and its axial location was established prior to the run by repositioning the shock generator. In the interaction region, surveys were obtained every 2 cm for the  $7.5^\circ$  generator tests and every 2.5 cm for the  $15^\circ$  generator tests. Downstream of the interaction the corresponding distances between survey stations were increased to 4 cm and 5 cm, respectively, for the two generator angles. In the reversed flow region established with the  $15^\circ$  generator, pitot measurements were obtained in upstream and downstream directions to help establish the extent of separation. When traversing the boundary layer, the probes were stopped at each location for a few seconds to avoid time lags in the measurements, and static pressures at the model surface were monitored continuously to verify interference-free data.

To verify that the model was aligned with the free-stream flow direction, surface-pressure measurements at selected axial positions were obtained at  $90^\circ$  intervals around the model, and skin-friction measurements at selected axial positions  $180^\circ$  apart. Comparisons of these data around the model showed variations that were within the experimental accuracy of the measurements. For the  $15^\circ$  generator tests, separation and reattachment lines around the model were also measured using a surface oil film technique. The results verified an axisymmetric separation zone.

A more complete description of the test procedure and data accuracy along with tabulations of all the test data are given in reference 11.

#### GOVERNING EQUATIONS AND NUMERICAL PROCEDURES

The equations and numerical procedures were first presented by the authors in reference 9. For completeness, some of that information is presented again in this section.

## Equations and Boundary Conditions

The mass-averaged Navier-Stokes equations for compressible flow, expressed in cylindrical coordinates with axial symmetry assumed, were used to predict the flow throughout the interaction region. The equations and the concept of mass averaging are discussed in reference 12. The turbulent Reynolds stress and heat-flux terms in these equations are related to the mean flow gradients of velocity and temperature by eddy-transport coefficients that are added to the molecular-transport coefficients. Additional restrictions on the equation system include the perfect gas assumption, constant specific heats, the Sutherland viscosity law, and zero bulk viscosity. The resulting equations are

$$\frac{\partial U}{\partial t} + \frac{\partial F}{\partial x} + \frac{\partial G}{\partial r} = H \quad (1)$$

$$U = r \begin{pmatrix} \rho \\ \rho u \\ \rho v \\ e \end{pmatrix} \quad F = r \begin{pmatrix} \rho u \\ \rho u^2 + \sigma_x \\ \rho uv + \tau_{xr} \\ (e + \sigma_x)u + \tau_{xr} v^2 + q_x \end{pmatrix} \quad (2)$$

$$H = \begin{pmatrix} 0 \\ 0 \\ \sigma_\theta \\ 0 \end{pmatrix} \quad G = r \begin{pmatrix} \rho v \\ \rho uv + \tau_{xr} \\ \rho v^2 + \sigma_r \\ (e + \sigma_r)v + \tau_{xr} u + q_r \end{pmatrix}$$

Figure 2 shows the computational domain. The conditions on the upstream boundary were prescribed by a combination of an inviscid, method of characteristics program (ref. 13), and a boundary-layer program (ref. 14) modified for turbulent flows by Marvin and Sheaffer. At the upstream boundary position, the experimental and computed incident shock waves were aligned and the boundary-layer program was run for an  $x$  distance that ensured a match of experimentally and numerically determined displacement thicknesses. Along the cylinder surface,  $r = r_w$  or  $y = 0$ , the boundary conditions used were the viscous, no-slip conditions,  $u = v = \partial p / \partial r = 0$ ,  $T = T_w$ , while along the outer boundary they were the inviscid, free-slip conditions,  $v = \partial p / \partial r = \partial u / \partial r = \partial T / \partial r = 0$ . At the downstream boundary the derivatives of all variables were set to zero, e.g.,  $\partial u / \partial x = 0$ . The initial conditions within the computational domain used to start the solutions were obtained by setting the values of all variables equal to their inflow boundary values at the same vertical station, that is,  $f(x, r, 0) = f(x_i, r, 0)$ ,  $x_i \leq x \leq x_f$ . To restart solutions or make modifications to turbulence parameters, initial values of the variables were set equal to their computed values obtained during the last time step of the previous solution.

## Numerical Procedures

The finite difference scheme used to solve equation (1) is the same as that developed originally by MacCormack (ref. 3) and applied more recently to two-dimensional turbulent shock boundary-layer interactions by Baldwin and MacCormack (ref. 15). The numerical techniques employed in the present study, along with all the pertinent difference equations, and some special procedures are reported in reference 9. The computational domain was subdivided into four subgrids with each subgrid divided into a number of uniform grid cells with spacing  $\Delta y$ . Finer spacing was employed near the wall. A total of 78 cells in the  $y$  direction was used; uniformly spaced grid with 48 cells in the  $x$  direction was used with spacing  $\Delta x = 0.80$  or  $0.635$  cm for the  $7.5^\circ$  and  $15^\circ$  cases, respectively. Some of the solutions presented later cover axial distances greater than those obtained with the 48 cells in the  $x$  direction. Those solutions were achieved by redefining the upstream boundary to coincide with a position about 3 cm ahead of the downstream boundary from converged solutions and then continuing the solutions on downstream for another 48 cell points in the  $x$  direction.

The solutions were advanced in time following the procedure described in reference 9. Steady-state convergence was assumed when solutions from at least 20 successive time steps showed little or no change. Computation times to achieve these fully converged solutions on a CDC 7600 were 3-4 hrs for the  $15^\circ$  generator cases and about 1 hr for the  $7.5^\circ$  cases.

## RESULTS AND DISCUSSION

### Experimentally Determined Flow-Field Features

Figure 2 depicts the major features of the shock-wave, boundary-layer interaction zone. The sketch is based on boundary-layer survey measurements and shadowgraphs taken during the experiments using both the  $7.5^\circ$  and  $15^\circ$  shock-wave generators. The incident shock wave, weakened and curved somewhat by the expansion fan emanating from the corner formed by the leading edge and the body of the shock-wave generator, impinges on the incoming boundary layer. The subsequent increases in surface pressure cause the boundary layer to thicken, or even separate in the case of the strongest incident shock wave, and induce a shock wave. Thereafter rapid flow turning and boundary-layer thinning occur and a recompression shock is formed.

Figure 3 shows the surface measurements obtained for the two shock-wave generator angles. Surface-pressure, skin-friction, and heat-transfer coefficients are shown as functions of a normalized interaction distance centered about  $x_0$ , the location of the intersection of the inviscid incident shock wave with the body surface in the absence of a boundary layer. With the  $7.5^\circ$  generator, the pressure rises continually through the interaction; the skin friction decreases initially in the presence of the adverse pressure gradient and rises thereafter in the recompression region where the boundary layer thins. The heat transfer follows a behavior similar to that of the pressure. No separation was observed in this case, either from the skin-friction mea-

surements or from oil-flow patterns that were established and photographed during some special tests. In contrast, with the  $15^\circ$  generator the initial increase in pressure levels off in a plateau, and negative values of skin friction were measured, both characteristics typically associated with separation. Rapid increases in pressure and skin friction occur downstream of reattachment. The heat transfer rises continually through the interaction until the surface pressure decreases. For both generator angles, the decay in pressure, skin friction, and heat transfer downstream of the interaction is a direct result of the expansion fan emanating from the corner of the generator.

Figures 4 and 5 present constant static pressure and velocity contours and illustrate further the details of the two interaction cases under investigation. The contours were constructed from the profiles of velocity and static pressure across the boundary layer obtained from pitot and static pressure and total temperature measurements taken at small  $\Delta x$  and  $\Delta y$  intervals. Complete tabulations of these profile data can be found in reference 11. Locations of the incident, induced, and recompression shocks are easily recognized in the pressure contours. Note that for the  $15^\circ$  generator the pressures are higher than the wall-peak pressure in the compression region downstream of the intersection of the incident and induced shocks. The velocity contours illustrate more dramatically the differences between the two flow cases. For the larger generator angle the flow velocity near the wall in the vicinity of the interaction is highly retarded and achieves negative values associated with the reversed flow in the separated zone.

A precise determination of separation and reattachment points for the separated case was made difficult because of the unsteady nature of the separated flow and the relatively large diameter of the skin friction element. A detailed discussion of this unsteady phenomenon is given in reference 9. A best estimate of the extent of the time-averaged separation region was obtained from data obtained with forward and backward facing pitot tubes. These data, obtained at fixed values of  $y$  with  $x$  varied by moving the shock generator, indicated a separated region extending from  $(x - x_0)/\delta_0 = -3.15$  to  $-1.68$ . This region is somewhat larger than the skin-friction measurements indicated. Locations of the separation and reattachment points from the pitot measurements are shown on the abscissa of the skin-friction plot.

#### Numerically Simulated Flow-Field Features

As previously mentioned, the turbulent Reynolds stress and heat-flux terms in equation (2) were assumed to be related to the mean flow gradients of velocity and temperature by algebraic eddy-transport coefficients that were simply added to the molecular-transport coefficients. Mainly, this choice was dictated by considerations of economy in the computer program. Although such a model may be restrictive in its application to other new flow situations, it suits our current objectives of (1) defining the eddy viscosity field that results when a shock impinges on a turbulent boundary layer, and (2) determining whether improvements in the eddy viscosity description used in the numerical simulations can be made by a close examination of the experimental data.

Results using a baseline turbulence model.—The first numerical simulations were obtained with a modified, two-layer, Cebeci-Smith (ref. 16) eddy viscosity model. Modifications suggested by Cebeci to account for pressure gradient effects were not used. The shear was expressed as

$$\tau = -\tau_{xr} = (\mu + \rho\epsilon) \left( \frac{\partial u}{\partial r} + \frac{\partial v}{\partial x} \right) \quad (3)$$

In the inner layer the following mixing length description for the eddy viscosity was used:

$$\epsilon = \epsilon_{\text{inner}} = \ell^2 \left( \left| \frac{\partial u}{\partial r} + \frac{\partial v}{\partial x} \right| \right) \quad (4)$$

where

$$\ell = \kappa y \left[ 1 - \exp\left(\frac{-y}{A}\right) \right] \quad (5)$$

$$A = A_w^+ \frac{\mu_w}{\sqrt{|\tau_w|} \rho_w} \quad (6)$$

with the Von Karman constant  $\kappa = 0.4$  and the Van Driest constant  $A_w^+ = 26$ . In the outer layer, the eddy viscosity was given, following Clauser, by

$$\epsilon = \epsilon_{\text{outer}} = 0.0168 \frac{u_{\text{max}} \delta_1^*}{I} \quad (7)$$

where

$$\delta_1^* = \int_0^{y_{\text{max}}} \left( 1 - \frac{u}{u_{\text{max}}} \right) \frac{r_w + y}{r_w} dy \quad (8)$$

$$I = 1 + 5.5 \left( \frac{y}{\delta} \right)^6 \quad (9)$$

$$\delta = 1.735 \delta_c^* \quad (10)$$

$$\delta_c^* = \int_0^{y_{\text{max}}} \left( 1 - \frac{\rho u}{(\rho u)_{\text{max}}} \right) \frac{r_w + y}{r_w} dy \quad (11)$$

The above definitions of the displacement thicknesses differ somewhat from the conventional ones. The present choice was dictated by the fact that, in the first stages of developing the Navier-Stokes code for the shock interaction

problem, overshoots in the velocity profiles during early time steps made it difficult to select the edge of the viscous layer. Therefore, the value of  $y_{\max}$  was simply taken as the boundary-layer thickness ahead of the interaction, and  $u_{\max}$  and  $(\rho u)_{\max}$  were taken as the local maximum values between the wall and  $y_{\max}$ . The boundary between the two layers was determined by the value of  $y$  where  $\epsilon_{\text{inner}} = \epsilon_{\text{outer}}$ .

The heat flux was expressed in terms of the eddy viscosity by

$$q = q_r = - \left( \frac{\mu}{Pr_r} + \frac{\rho \epsilon}{Pr_t} \right) c_p \frac{\partial T}{\partial r} \quad (12)$$

where  $Pr_t = 0.9$ .

Results of the computations using this baseline turbulence model are compared with the experimental data in figures 6, 7, and 8. Overall, the computations predict the qualitative features of the two flows remarkably well considering the simplicity of the turbulence model, but a closer examination of the comparisons points out the major limitations of the computations.

The overall surface pressure rise for the flow with the  $7.5^\circ$  shock-wave generator (fig. 6a) is predicted reasonably well, except for the location of the initial rise in pressure. The corresponding predicted rises in both skin friction and heat transfer lag the data in the interaction region, reflecting the inability of the simple turbulence model to predict any upstream influence, but the final predicted levels downstream agree reasonably well with the data. The skin friction prediction shows separation at the surface but the measurements do not. The pressure contour comparisons (fig. 7a) show that the computation predicts only the incident and reflected shocks whereas the experimental data show the presence of an induced shock. The comparison of the streamline contours (fig. 8a) shows the prediction of a zero velocity line just off the surface accompanied by a small region of reversed flow which is not present in the experimental data.

Similar conclusions can be made from comparisons of the numerical computations and the data for the flow with the  $15^\circ$  shock-wave generator (figs. 6b, 7b, and 8b). With the baseline turbulence model, no upstream influence is predicted and in this separated flow case no plateau pressure is predicted. The induced shock wave caused by the large separation in the experiment is not predicted because the computation predicts such a small separation height. For this separated flow case, the baseline turbulence model results in good prediction of the overall pressure and skin friction rises and their subsequent decay; but the heat transfer is substantially underpredicted (see fig. 6b).

Baseline model modifications.—Attempts were made to guide changes in the turbulence model by combining data analysis and trial and error solutions in the actual Navier-Stokes code. Ideally, these changes could have been guided entirely from data if absolutely reliable shear-stress measurements had been available. But, since attempts to directly measure the shear stress through these interactions have so far produced unsatisfactory results, the boundary-

layer profile data were used. A significant degree of uncertainty is introduced in this procedure, however, because the inertial forces dominate the momentum balance, especially in the outer portions of the flow. Conversely, relying solely on trial and error solutions to the code itself to guide modeling changes would be time consuming and perhaps unsuccessful if attention was not confined to physically meaningful changes.

The shear-stress and heat-flux distributions through the boundary layer were evaluated by the use of experimental profile data to solve the following equations based on the boundary-layer approximation:

$$\tau = \frac{1}{(r_w + y)} \left[ r_w \tau_w + \frac{\partial}{\partial x} \int_0^y (r_w + y)(p + \rho u^2) dy - u \frac{\partial}{\partial x} \int_0^y (r_w + y) \rho u dy \right] \quad (13)$$

and

$$q - u\tau = \frac{1}{(r_w + y)} \left[ r_w q_w + c_p T_t \frac{\partial}{\partial x} \int_0^y (r_w + y) \rho u dy - \frac{\partial}{\partial x} \int_0^y (r_w + y) \rho u c_p T_t dy \right] \quad (14)$$

By performing integration with respect to  $y$  before differentiation with respect to  $x$  and by employing the conservative form of the variables, for example  $(p + \rho u^2)$ , it was expected that errors in the momentum and energy balances could be minimized. Despite these precautions, not all the shear profiles approached zero at large distances from the wall where they should have. In some of these cases it was possible to adjust the inertial balance across the boundary layer so that zero shear was achieved at the edge of the thermal boundary layer. These adjustments were usually small for the  $7.5^\circ$  shock wave generator profiles, but somewhat larger for the  $15^\circ$  generator profiles.

Figure 9 shows the shear profiles resulting from these momentum and energy balances for axial locations ahead, within, and downstream of the two interaction regions. For the flow with the  $7.5^\circ$  generator the maximum shear stress within the boundary layer builds up rapidly within the interaction region as the adverse pressure gradient increases; after peak pressure is reached this maximum shear relaxes toward its initial level but at a very slow rate. At the farthest downstream location where the pressure gradient is favorable the shear near the wall decreases and subsequently increases, indicating that the shear in the outer extremes of the boundary layer is adjusting to the local flow gradients more slowly than the shear near the wall. Similar

conclusions can be reached for the separated case using the 15° generator. In this case, data were available for a larger downstream interaction distance, and the shear appears to have adjusted to the local flow gradients. Also, for this separated case, the maximum shear in the boundary layer continues to increase downstream of reattachment and slightly beyond the location of peak pressure.

A maximum mixing length was determined at each of the profile survey stations by dividing the experimentally deduced shear distributions by the measured velocity gradients, plotting the results, and choosing the maximum value of mixing length. For those cases where the mixing length continuously increased with distance from the wall, the value of maximum mixing length was chosen at the point where the first significant departure from a linear mixing length distribution occurred. These maximum values are shown in figure 10 as a function of the interaction length parameter. The extremes on the bars represent the uncertainty introduced by using shear profiles evaluated either directly from the momentum balances or from momentum balances modified by adjusting the inertial terms to insure zero shear at the edge of the thermal boundary layer. The uncertainty was largest in the region downstream of reattachment for the 15° generator case. In both cases the maximum mixing lengths tend to decrease in regions of adverse pressure gradient, where the boundary layer thickens, and to increase in regions of favorable pressure gradient.

Near the surface where the importance of the inertia and convection terms in the momentum and energy balances diminished, attempts were made to evaluate  $\kappa$  and  $A_w^+$ . The shear profiles at each survey station were analyzed by integrating the following system of equations to obtain values of velocity and temperature as a function of  $y$  out to distances where the estimated errors in the inertial balance became significant compared to the magnitude of the local shear (usually this consisted of about 9 measured points away from the wall):

$$\tau = \left( \mu + \rho \ell^2 \left| \frac{\partial u}{\partial y} \right| \right) \frac{\partial u}{\partial y} \quad (15)$$

$$\ell = \kappa y \left[ 1 - \exp\left(\frac{-y}{A}\right) \right] \quad (16)$$

$$A = \frac{\mu_w}{\sqrt{|\tau_w| \rho_w}} A_w^+ \quad (17)$$

$$q = - \left( \frac{\mu}{Pr} + \frac{\rho \ell^2}{Pr_t} \left| \frac{\partial u}{\partial y} \right| \right) \frac{\partial T}{\partial y} \quad (18)$$

Best fits to the velocity and temperature profile data near the wall were achieved by repeated integration of these equations until the sum of the root mean square of the differences between the predicted and measured velocities and temperatures was minimized. The procedure was automated for solution on a CDC 7600 and initiated by inputting shear and temperature profiles from the

momentum and energy balances along with the measured values of wall shear. An optimization routine (described in ref. 16) was initiated and values of  $\kappa$  and  $A_w^+$  and  $q_w$  were sought to satisfy the minimization criteria. (This optimization routine was developed by Garret N. Vanderplaats, of NASA Ames, who helped to implement it for the present application.) The root mean square of the residuals never exceeded 5% and in most cases was less. Exceptions to this residual band occurred for the 15° generator case in the separated region. However, it was still possible to achieve this band at these profile stations, provided the input wall shear was also considered part of the optimization routine along with the other parameters. This was not surprising, however, since accurate skin-friction measurements were difficult to make in this separated region. Examples of the best fits to the velocity and temperature data near the upstream edge of the separated region are shown as the solid lines in figure 11. Two important aspects of this example are noteworthy. First, at this station, the wall shear needed to achieve a best fit was  $-5.28 \text{ N/m}^2$  whereas the direct measurement was  $12.1 \text{ N/m}^2$ . Considering that the station is near the separation point where experimental accuracy is poor and that the separation point is unsteady, this disparity is not unreasonable. Second, at this station, values of  $\kappa$  and  $A_w^+$  are significantly lower than their corresponding undisturbed values, 0.4 and 26.

Figure 12 presents the values of  $\kappa$  and  $A_w^+$  required to achieve these best fit velocity and temperature profiles for both of the interaction cases being studied. The error bands on the symbols again represent the uncertainty introduced by using shear profiles evaluated either directly from the momentum balances or from momentum balances modified by adjusting the inertial terms to insure zero shear at the edge of the thermal boundary layer. The results for the 7.5° generator show that  $A_w^+$  decreases in the vicinity of the interaction while  $\kappa$  increases. These results are interpreted as indicating a higher eddy viscosity throughout the region than that predicted by the baseline turbulence model. This could explain why the numerical simulations using the baseline turbulence model predicted separation. For the 15° generator case where separation was present, similar trends in  $\kappa$  and  $A_w^+$  are apparent. However, the uncertainties within the separated region precluded any precise determination of the parameters. Apparently, both  $\kappa$  and  $A_w^+$  decrease ahead of and in the upstream portions of the separated region. At the downstream edge of the separated region near reattachment  $\kappa$  has increased considerably and  $A_w^+$  is also increasing. The physical interpretation of these results suggests that ahead of separation the sublayer or inner region has a somewhat higher eddy viscosity than the baseline model would predict, but in the logarithmic region the viscosity is somewhat lower than the baseline model would predict. In the separated region, an interpretation is more difficult to arrive at, but apparently, at least near the reattachment point, the eddy viscosity is higher across the sublayer and logarithmic regions than would be predicted by the baseline model.

The turbulence model mixing length formulation suggested by the foregoing data analysis was introduced into the Navier-Stokes computer code in the following way:

$$\tau = -\tau_{xr} = (\bar{\mu} + \rho \epsilon) \left( \frac{\partial u}{\partial r} + \frac{\partial v}{\partial x} \right) \quad (19)$$

$$\epsilon = \ell^2 \left[ \left( \frac{\partial u}{\partial r} \right)^2 + \left( \frac{\partial v}{\partial x} \right)^2 \right]^{1/2} \quad (20)$$

In the inner region

$$\ell = \kappa(x) \left[ 1 - \exp\left(\frac{-y}{A}\right) \right] \quad (21)$$

$$A = A_w^+(x) \frac{H_w}{\sqrt{|\tau_w|} \rho_w} \quad (22)$$

In the outer region

$$\ell = \ell_{\max}(x) \quad (23)$$

Employing  $\ell_{\max}$  in this model formulation eliminated the need for arbitrarily defining compressible and incompressible displacement thickness as was the case with the baseline model. The boundary between the two regions is determined by the value of  $y$  where  $\ell = \ell_{\max}$ . The heat flux equation remained the same as for the baseline model (see eq. 12).

Computer simulations were next obtained using the experimental data analysis as a guide for evaluating the parameters  $\ell_{\max}(x)$ ,  $\kappa(x)$ , and  $A_w^+(x)$ . First, values directly from the data analysis were used. Examination of the resulting computer simulations made it apparent that adjustments to the parameters would be needed before the simulations would predict the experimentally determined features of the flow fields in the interaction region. Therefore, a trial and error procedure was initiated to arrive at more appropriate distributions of the turbulence parameters. The procedure is still underway at this time. Before discussing the results of this procedure to date, some interesting observations can be pointed out. The simulations were all more sensitive to modifications of the inner region model parameters than the outer maximum mixing length parameter. In the inner region itself,  $A_w^+(x)$  modifications tended to affect the solutions more than those for  $\kappa(x)$ , especially in the separated case. However, best results have been achieved with modification to both  $A_w^+(x)$  and  $\kappa(x)$ .

Results using a modified turbulence model.—The turbulence parameter variations used in the latest computer simulations employing the complete Navier-Stokes equations are shown as the solid and dashed lines in figures 10 and 12. The maximum mixing length variation (fig. 10), employed in all simulations, corresponded to the mean variation exhibited by the data analysis. In the inner layer region (fig. 12), values of  $A_w^+$  and  $\kappa$  had to be altered to obtain better predictions of the experimental surface and flow-field data. For the 7.5° generator case these variations in  $A_w^+$  and  $\kappa$  follow the trends exhibited by the data analysis. The largest disparity between the values used in the

simulations and those deduced from data analysis is in  $A_w^+$  at the beginning of the interaction region. As noted before, decreasing  $A_w^+$  and increasing  $\kappa$  both result in a larger eddy viscosity in the inner layer region. For the  $15^\circ$  generator case the variations in the inner layer turbulence parameters follow the same trends as the data analysis except near reattachment. Part of the reason for this disparity is that the data analysis in this region was completed only recently and there was insufficient time to obtain converged simulations before preparing this manuscript.

2007001 517

The results of the computer simulations using the turbulence parameter variations described above are presented in figures 6, 7, and 8. For the  $7.5^\circ$  generator case there is obvious improvement over the baseline predictions of skin friction and heat transfer in the interaction region (see fig. 6a). Separation is not predicted and the upstream influence of the interaction coincides with that observed from the data. Downstream of the peak pressure location the heat-transfer prediction is not as good as the baseline model predictions, but this could be explained by an incorrect choice of a constant turbulent Prandtl number. At this stage of model development this disparity in heating prediction is not considered crucial because the solutions of the momentum and energy equations are loosely coupled. The turbulence model changes had little effect on the surface pressure prediction. The pressure and velocity contours (figs. 7 and 8) are not changed significantly from those for the baseline model, except that no reversed flow region is predicted with the modified model. The reflected shock observed in the data is still not predicted. The main reason for this is that the numerical simulations fail to show a significant thickening of the boundary layer at the start of the interaction region.

Results using the turbulence model modifications for the  $15^\circ$  generator case are also shown in figures 6, 7, and 8. The predicted separation bubble size increased considerably with a corresponding prediction of upstream influence and a plateau in the surface pressure. The pressure contours show the presence of an induced shock wave similar to that observed in the experiment. Obviously, substantial deficiencies still exist in the prediction using the modified model. The separated bubble size is still smaller in height than the experiment indicates; the plateau pressure is only about half the measured value; and all three surface quantities show substantial differences with the measurements in the interaction region. It is felt, however, that a significant improvement in the surface predictions can be made by including the latest data analysis values of  $A_w^+$  and  $\kappa$  near reattachment. This should shorten the extent of predicted separation and shift the rise in skin-friction and heat-transfer upstream.

#### CONCLUDING REMARKS

A detailed experimental investigation of the mean flow throughout two shock-wave boundary-layer interaction regions, one with separation and one without, has been presented. Although the interactions were very complex, the mean data were of sufficient detail and quality to assess the validity of numerical simulations and to guide turbulence model changes.

Numerical solutions, employing the full time-averaged Navier-Stokes equations along with algebraic eddy-viscosity models appropriate for zero-pressure-gradient flows, predicted the overall features of the flow fields, but they were seriously deficient in predicting the details of the interaction regions. Through a combination of data analysis and trial and error computer simulations, which tested the sensitivity of the solutions to turbulence model parameter changes, the agreement between numerical predictions and experiment was improved.

Although the improvements fell short of identifying an optimum model, several important trends regarding the two-layer, algebraic eddy-viscosity model can be noted. The inner layer model parameters had substantially more influence on the numerical simulations than the outer layer parameter. Where the boundary layer was unseparated, the eddy viscosity in the inner layer region had to be increased substantially over that predicted by a zero-pressure-gradient, two-layer model; otherwise separation was predicted. Therefore the simple zero-pressure-gradient model cannot be used to predict locations of separation. Where separation did occur, the results were less clear, but the eddy viscosity in the sublayer region had to be increased while in the logarithmic region it had to be reduced somewhat; otherwise the separation bubble size was substantially underpredicted.

#### REFERENCES

1. Ballhaus, W. F., and Bailey, F. R.: Numerical Calculation of Transonic Flow About Swept Wings. AIAA Paper 72-677, June 1972.
2. Rakich, J. V., and Kutler, P.: Comparison of Characteristics and Shock Capturing Methods with Application to the Space Shuttle Vehicle. AIAA Paper 72-191, Jan. 1972.
3. MacCormack, R. W.: Numerical Solution of the Interaction of a Shock Wave with a Laminar Boundary Layer. Lecture Notes in Physics, Vol. 8, Springer Verlag, New York, 1971, p. 151.
4. Hung, M., and MacCormack, R. W.: Supersonic and Hypersonic Laminar Flows Over a Two-Dimensional Compression Corner, AIAA Paper 75-2, Jan. 1975.
5. Baldwin, B. S., and MacCormack, R. W.: Numerical Solution of a Strong Shock Wave with a Hypersonic Turbulent Boundary Layer. AIAA Paper 74-558, June 1974.
6. Wilcox, D. C.: Numerical Study of Separated Turbulent Flows. AIAA Paper 74-584, June 1974.
7. Deiwert, G. S.: Numerical Simulation of High Reynolds Number Transonic Flows. AIAA Paper 74-603, June 1974.

8. Redda, D. C., and Murphy, J. D.: Shock Wave Turbulent Boundary Layer Interactions in Rectangular Channels, Part II: The Influence of Sidewall Boundary Layers on Incipient Separation and Scale of the Interaction. AIAA Journal, vol. 11, no. 10, Oct. 1973, pp. 1367-1368.
9. Horstman, C. C., Kussoy, M. I., Coakley, T. J., Rubesin, M. W., and Marvin, J. G.: Shock Wave Induced Turbulent Boundary-Layer Separation at Hypersonic Speeds. AIAA Paper 75-4, Jan. 1975.
10. Horstman, C. C., and Owen, F. K.: Turbulent Properties of a Compressible Boundary Layer. AIAA Journal, vol. 10, no. 11, Nov. 1972, pp. 1418-1424.
11. Kussoy, M. I., and Horstman, C. C.: An Experimental Documentation of a Hypersonic Shock-Wave Turbulent Boundary-Layer Interaction Flow—With and Without Separation. NASA TM X-62,412, 1975.
12. Rubesin, M. W., and Rose, W. C.: The Turbulent Mean-Flow Reynolds-Stress, and Heat Flux Equations in Mass-Averaged Dependent Variables. NASA TM X-62,248, March 1973.
13. Sorensen, V. L.: Computer Program for Calculating Flow Fields in Supersonic Inlets. NASA TN D-2897, July 1965.
14. Marvin, J. G., and Sheaffer, Y. S.: A Method for Solving the Nonsimilar Boundary-Layer Equations Including Foreign Gas Injection. NASA TN D-5516, Nov. 1969.
15. Baldwin, B. S., and MacCormack, R. W.: Interaction of Strong Shock Wave with Turbulent Boundary Layer. Proceedings of the 4th International Conference on Numerical Methods in Fluid Dynamics, Boulder, Colorado, June 1974.
16. Vanderplaats, Garret N.: CONMIN - A FORTRAN Program for Constrained Function Minimization User's Manual. NASA TM X-62,282, August 1973.

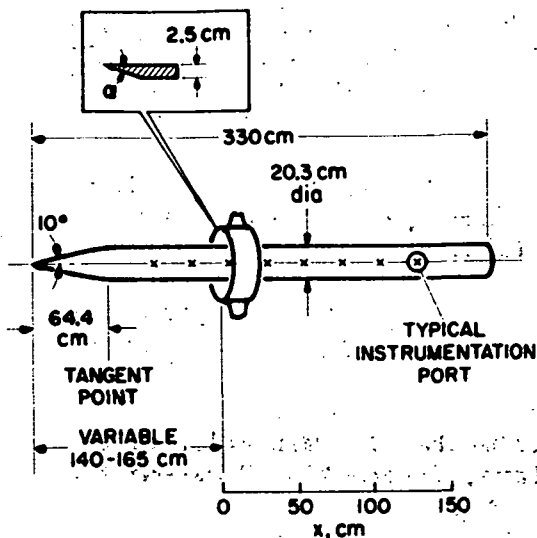


Figure 1.- Test model.

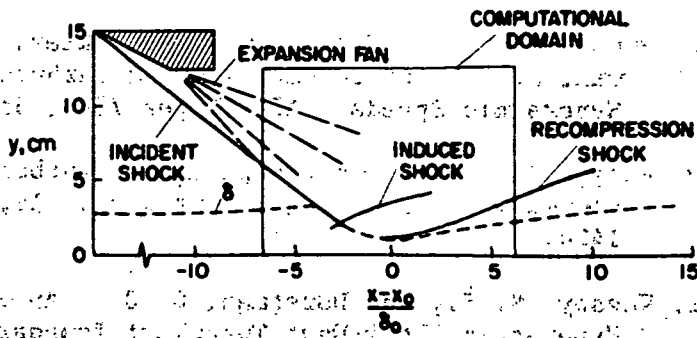


Figure 2.- Flow-field sketch and computational domain.

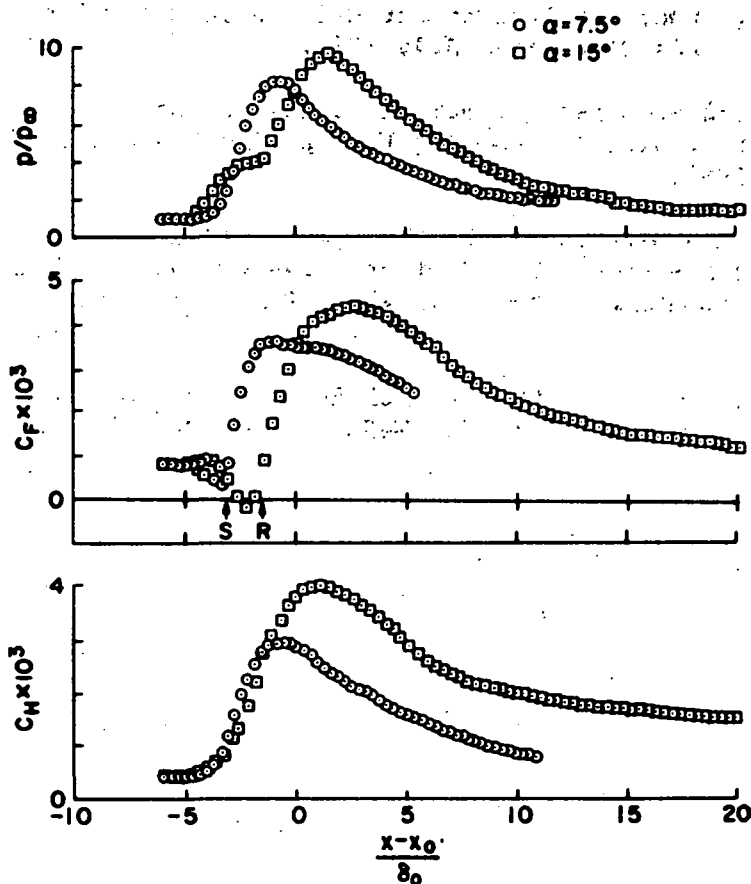


Figure 3.- Measurements along the model surface.

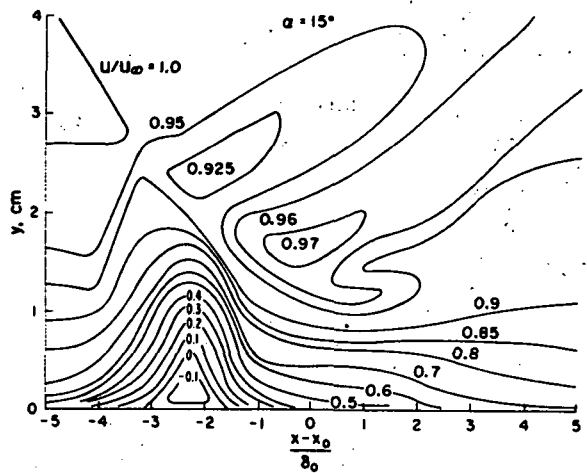
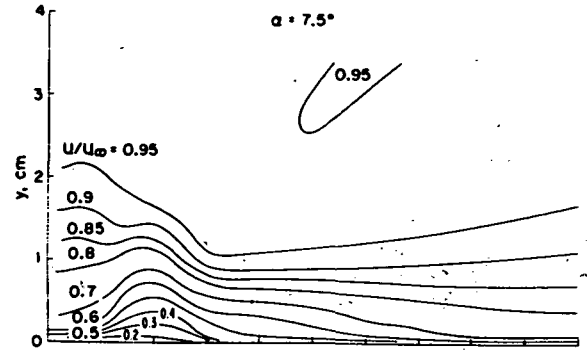
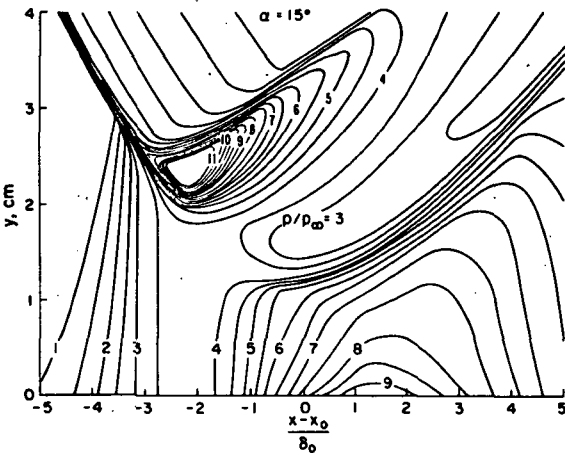
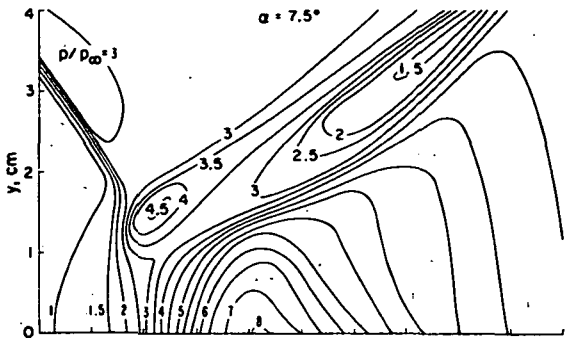
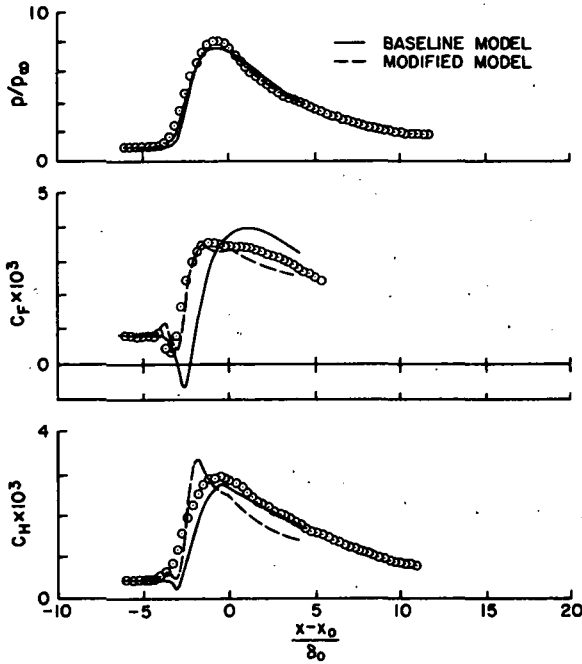
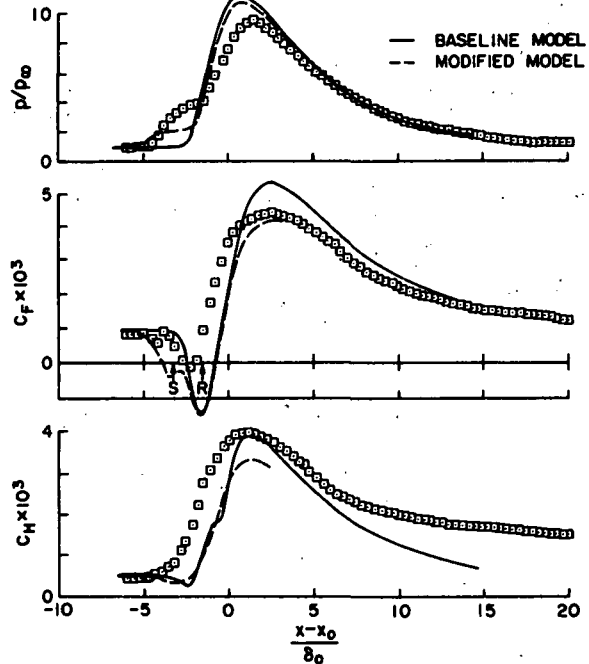


Figure 4.- Static pressure contours obtained from flow-field measurements.

Figure 5.- Velocity contours obtained from flow-field measurements.

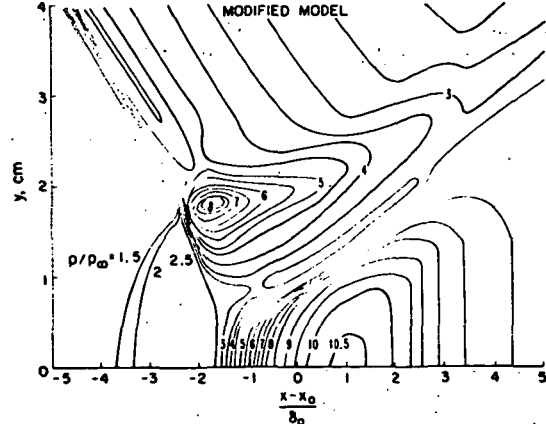
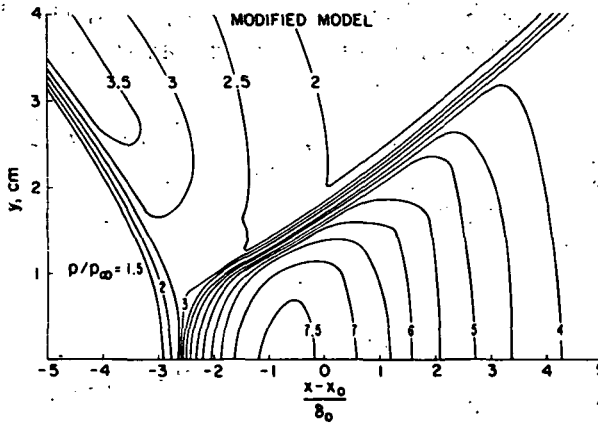
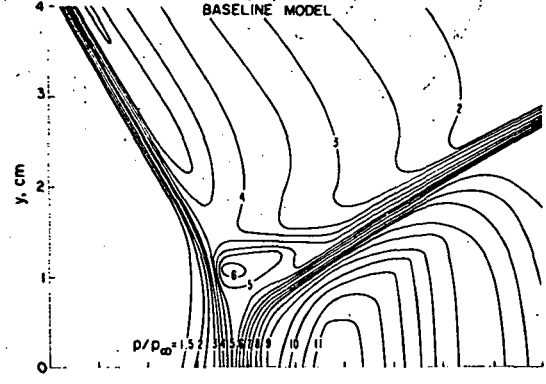
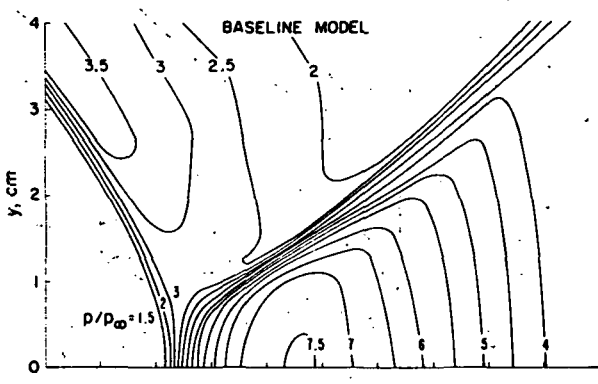
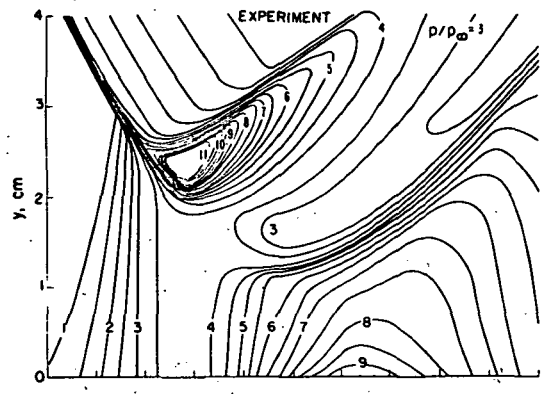
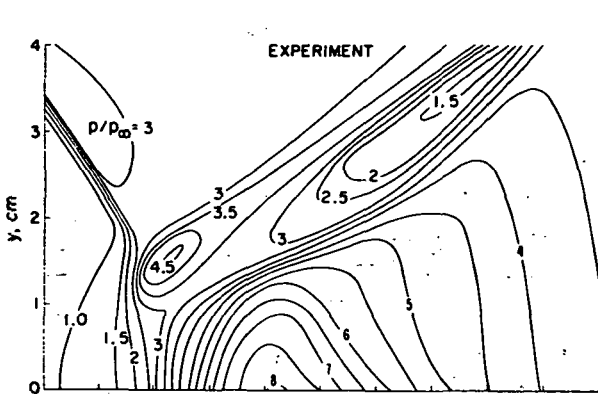


(a)  $\alpha = 7.5^\circ$ .



(b)  $\alpha = 15^\circ$ .

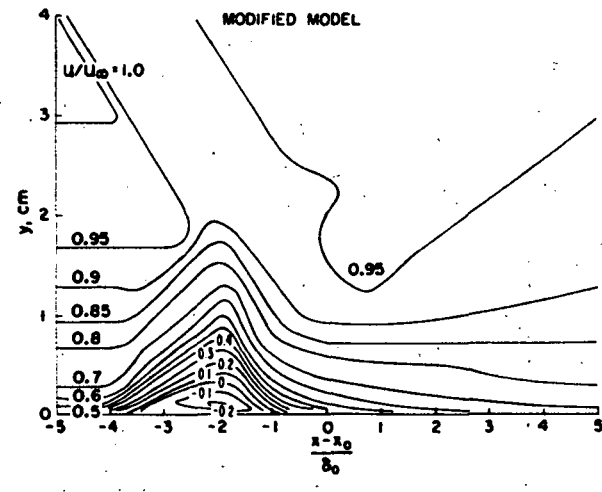
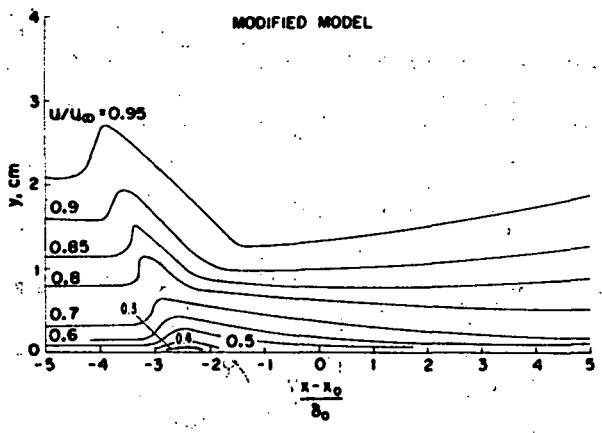
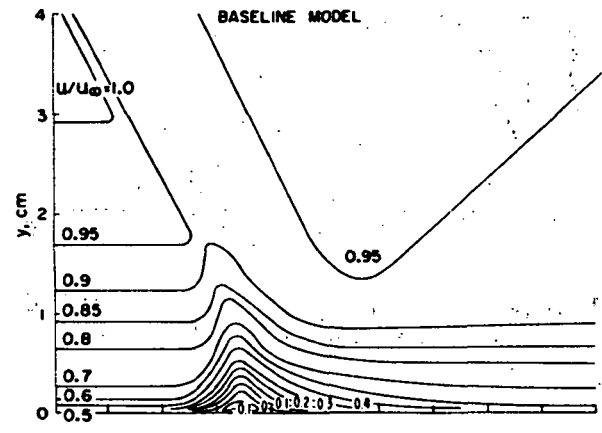
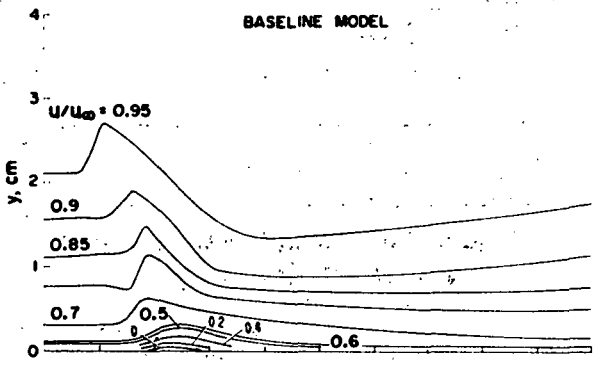
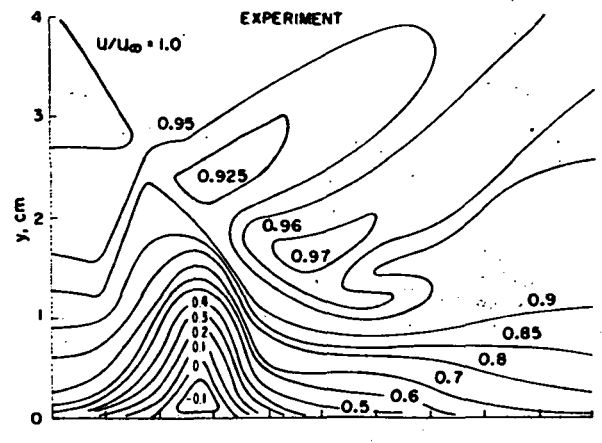
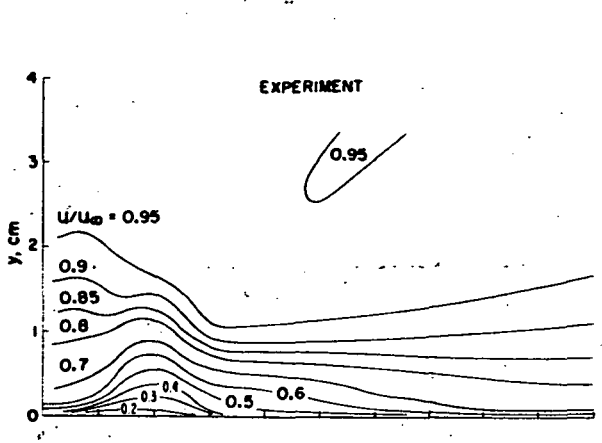
Figure 6.- Comparisons of computations and measurements along the model surface.



(a)  $\alpha = 7.5^\circ$ .

(b)  $\alpha = 15^\circ$ .

Figure 7.- Comparisons of static pressure contours from computations and experiment.



(a)  $\alpha = 7.5^\circ$ .

(b)  $\alpha = 15^\circ$ .

Figure 8.- Comparisons of velocity contours from computations and experiment.

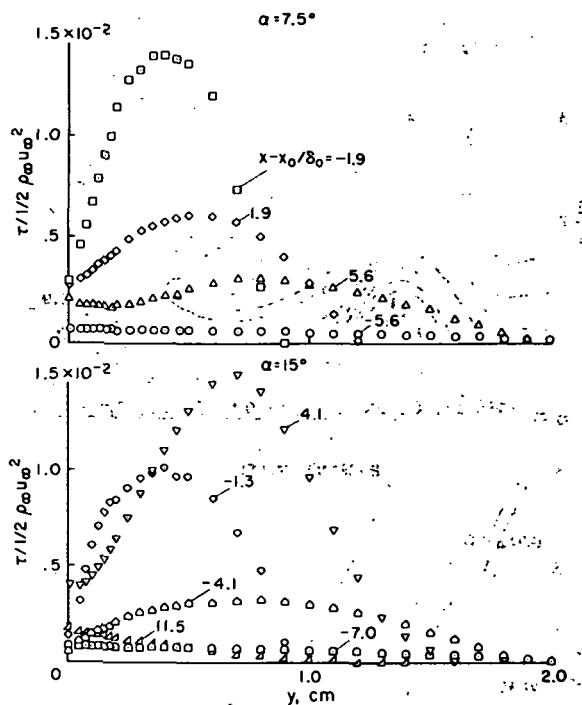


Figure 9.- Shear profiles for various axial locations along the model.

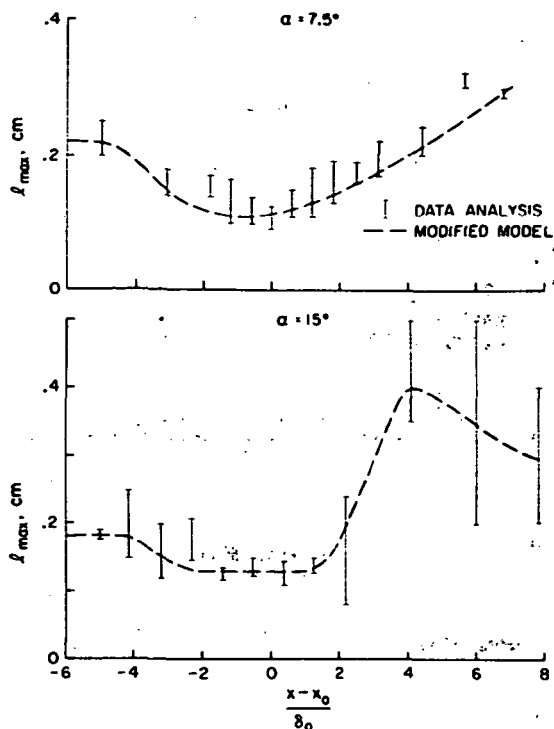


Figure 10.- Axial variation of maximum mixing lengths.

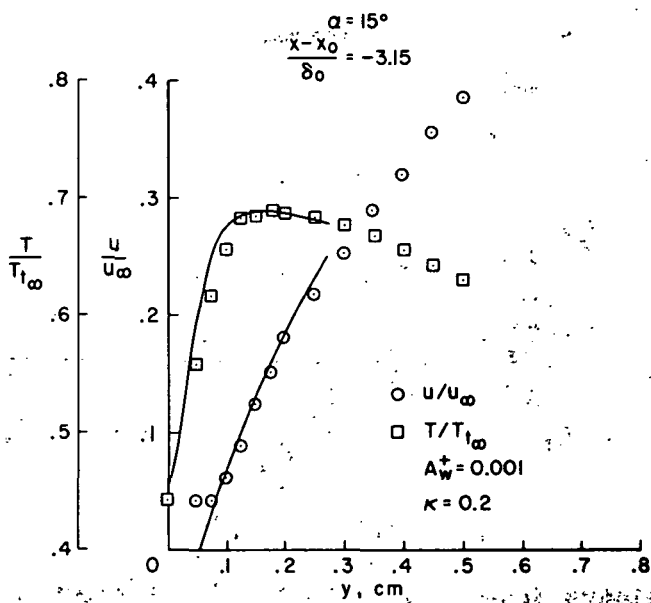


Figure 11.- Comparison of experimental and best fit velocity and temperature profiles employing a modified inner eddy-viscosity model.

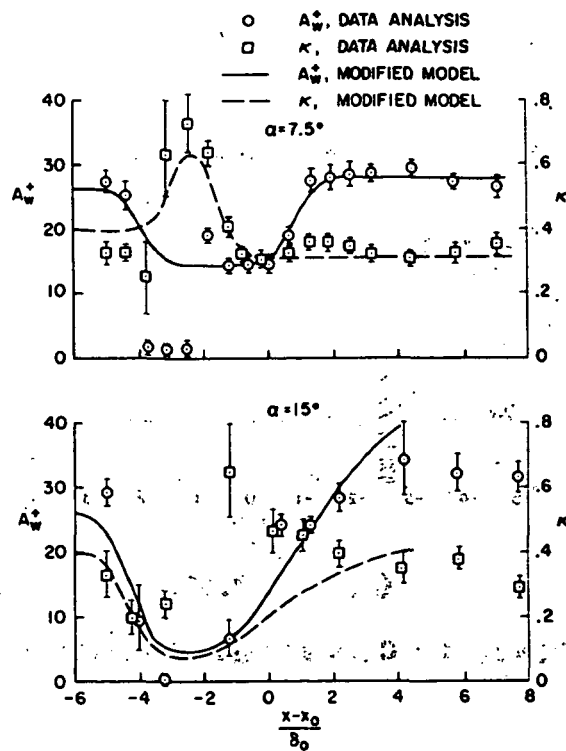


Figure 12.- Axial variation of  $A_w^+$  and  $\kappa$ .